

ARTICLE OPEN



Global response of upper-level aviation turbulence from various sources to climate change

Soo-Hyun Kim¹✉, Jung-Hoon Kim¹✉, Hye-Yeong Chun² and Robert D. Sharman³

Atmospheric turbulence at commercial aircraft cruising altitudes is a main threat to aviation safety worldwide. As the air transport industry expands and is continuously growing, investigating global response of aviation turbulence under climate change scenarios is required for preparing optimal and safe flying plans for the future. This study examines future frequencies of moderate-or-greater-intensity turbulence generated from various sources, viz., clear-air turbulence and mountain-wave turbulence that are concentrated in midlatitudes, and near-cloud turbulence that is concentrated in tropics and subtropics, using long-term climate model data of high-emissions scenario and historical condition. Here, we show that turbulence generated from all three sources is intensified with higher occurrences globally in changed climate compared to the historical period. Although previous studies have reported intensification of clear-air turbulence in changing climate, implying bumpier flights in the future, we show that intensification of mountain-wave turbulence and near-cloud turbulence can also be expected with changing climate.

npj Climate and Atmospheric Science (2023)6:92; <https://doi.org/10.1038/s41612-023-00421-3>

INTRODUCTION

Atmospheric turbulence in the upper troposphere and lower stratosphere (UTLS) is the leading cause of weather-related accidents and incidents for commercial aircraft^{1,2}. Encountering unexpected turbulence can cause injuries to flight attendants and passengers and structural damage to aircraft, and can lead to flight delays and extra fuel burns due to increasing flight times incurred with turbulence avoidance. Turbulence with scales of a few 100 m—a few km that directly cause aircraft bumpiness is categorized into three distinct types based on their generation mechanism and location^{1,3,4}: clear-air turbulence (CAT), mountain-wave turbulence (MWT), and convectively-induced turbulence (CIT).

CAT is associated with large-scale generation mechanisms such as the upper-level jets and fronts⁵ and spontaneous balance adjustment with gravity wave emission in the vicinity of the jet-exit region⁶. MWT is related to large-amplitude gravity waves and their breaking above mountainous terrain. Vertically propagating mountain waves disturb the background fields, which can provide favorable conditions for MWT, and the breaking of mountain waves directly leads to small-scale turbulence⁷. CIT occurs within cloud, as well as near the cloud boundaries, but sometimes can occur at substantial vertical and horizontal distances away from the cloud boundary⁸. CIT within cloud is to be expected but may be avoidable within air traffic control constraints by use of aircraft radar or remote-sensing observations such as radar and satellite data, while CIT out of cloud occurring in the cloud-free air is invisible to pilots, and is difficult to avoid. In particular, CIT above the cloud boundary (hereafter termed near-cloud turbulence, NCT) can be caused by shear and convective instabilities, deformation of convectively induced flows, and convectively induced gravity waves and their breaking^{1,9–11} and has been shown to be responsible for some UTLS turbulence encounters^{10,12–17}.

Due to limitations in computational resources to explicitly forecast turbulence, aviation-scale turbulence has been predicted

from larger scale disturbances resolvable in current numerical weather prediction (NWP) models^{4,18–20} based on the assumption of a downscale cascade process²¹ to turbulence scales. Current operational turbulence forecasting methods, e.g., the Graphical Turbulence Guidance^{18,19,22} and Korean Turbulence Guidance²³ products, estimate turbulence “potential”, i.e., the magnitude of turbulence intensity diagnosed by turbulence indices, using NWP-based multiple turbulence diagnostics such as the Ellrod indices^{24,25}, flow deformation²⁵, Brown indices²⁶, etc. The state-of-the-art GTG predicts MWT using turbulence indices which combine a two-dimensional near-surface mountain-wave parameter and three-dimensional CAT diagnostics¹⁹. Recently, NCT diagnostics have also been developed based on the parameterization of convective gravity waves (convective gravity wave drag, CGWD)¹¹ and their feasibility was validated against global in situ flight data²⁷.

There have been several climate model-based studies that investigated the impacts of climate change on CAT, and all studies consistently showed that CAT is expected to increase strongly in a changing climate^{28–31}. For example, Williams and Joshi (2013)³¹ found a 40–170% increase in the frequency of moderate-or-greater (MOG)-intensity CAT at 200 hPa during the Northern Hemisphere winter in the North Atlantic flight corridor. Extending the previous studies^{30,31}, Storer et al. (2017)²⁹ investigated the response of CAT to changing climate in two vertical layers (200 and 250 hPa), in all seasons, for multiple turbulence intensity categories (five levels). It was found that the MOG-intensity CAT over some midlatitude regions, such as Europe and the North Atlantic, increased by more than 100% in the future scenario experiment²⁹. However, to date, there have been no studies of the impacts of climate change on NCT and MWT frequencies. Here, we examine how global warming and climate change affect aviation turbulence by considering not only CAT but also MWT and NCT. Our assessments are based on outputs from the second version of the Norwegian Earth System

¹School of Earth and Environmental Sciences, Seoul National University, Seoul, South Korea. ²Department of Atmospheric Sciences, Yonsei University, Seoul, South Korea.

³National Center for Atmospheric Research, Boulder, CO, USA. ✉email: kimsh12@snu.ac.kr; jhkim99@snu.ac.kr

Table 1. Descriptions of turbulence diagnostics used in this study.

Diagnostic	Description
(a) CAT diagnostics^{18,19}	
Speed	Horizontal wind speed
Brown1	Simplified Richardson number (Ri) tendency
Brown2	The cube root of energy dissipation rate (EDR) from simplified Richardson number tendency
Ellrod1	The product of vertical wind shear and deformation
Ellrod2	Vertical wind shear multiplied by the difference between deformation and horizontal divergence
Ellrod3	Ellrod2 with divergence tendency substituted for horizontal divergence
VWS	Vertical shear of horizontal wind
NGM1	Wind speed multiplied by deformation
NGM2	Magnitude of vertical temperature gradient multiplied by deformation
iawind	Inertial advective wind
DEF ²	Total deformation squared
DIV	Magnitude of horizontal divergence
VORT ²	Vertical vorticity squared
LHFK	Lighthill-Ford spontaneous imbalance
NVA	Negative vorticity advection
F2D	Two-dimensional frontogenesis function on z-surface
F3D	Three-dimensional frontogenesis function on z-surface
TEMPG	Absolute value of horizontal temperature gradient
1/Ri _{dry}	Inverse Ri (dry air)
CP	Colson-Panofsky turbulent kinetic energy
Endlich	Wind speed multiplied by turning
DTF3	Diagnostic turbulent kinetic energy-epsilon formulation
PVGRAD	Horizontal potential vorticity gradient
1/Ri _{moist}	Inverse Ri (moist air)
w ² /Ri	Vertical velocity squared divided by Ri
NCSU1	Absolute value of advection multiplied by vorticity gradient divided by Ri
NCSU2	Magnitude of vorticity gradient multiplied by gradient of Montgomery stream function
Dutton	Dutton's empirical index
EDRLUN	EDR from simplified Ri tendency
EDRLL	EDR squared from second-order structure function
(b) MWT diagnostics¹⁹	
Diagnostic	Description
MWT1	$d_s \times w^2/Ri$
MWT2	$d_s \times \text{CTSQ}$ (temperature structure constant estimated from longitudinal and transverse second-order structure functions of air temperature)
MWT3	$d_s \times F3D$
MWT4	$d_s \times \text{Speed}$
MWT5	$d_s \times DIV $
MWT6	$d_s \times \text{NGM1}$
MWT7	$d_s \times \text{SIGWAVG}$ (variance of vertical wind estimated from average of longitudinal and transverse second-order structure function)
MWT8	$d_s \times \text{LHFK}$ divided by Ri
MWT9	$d_s \times \text{iawind}$
MWT10	$d_s \times \text{EDRAVG}$ (EDR squared estimated from average of longitudinal and transverse second-order structure functions)
MWT11	$d_s \times \text{SCHGW}$ (EDR from variance of vertical velocity)
MWT12	$d_s \times \text{TEMPG} $
MWT13	$d_s \times \text{DEF}^2$
MWT14	$d_s \times \text{EDRLL}$
(c) NCT diagnostics^{11,27}	
Diagnostic	Description
CGWD	Absolute value of convective gravity wave drag
EDR _{CGWD}	EDR estimated from CGWD and background wind and stability

The description of the 46 turbulence diagnostics [(a) 30 CAT, (b) 14 MWT, and (c) 2 NCT] used. Each turbulence diagnostic is computed using outputs from the historical and high-emissions (SSP5-8.5) scenarios.

(NorESM2-MM³²) forced by the Shared Socioeconomic Pathway (SSP) 5–8.5 (SSP5-8.5) scenario (see Methods).

RESULTS

In this study, the 45-year daily-mean data obtained from both historical (1970–2014) and high-emissions (SSP5-8.5; 2056–2100) scenarios are used. Using these models as meteorological input, we calculate 30 CAT diagnostics¹⁹, 14 MWT diagnostics¹⁹, and 2 NCT diagnostics²⁷ listed in Table 1 using daily-mean wind (zonal, meridional, and vertical wind), air temperature, relative humidity, cloud water/ice mixing ratio, and geopotential height between 200 and 250 hPa and terrain height (see Methods). Note that the MWT diagnostics are computed only over mountain-wave prone areas that are defined using the model terrain height¹⁹, and the NCT diagnostics are computed only at grid points above where the model predicts convective clouds exist²⁷.

Figure 1 demonstrates the spatial distributions of the 45-year seasonally averaged horizontal wind speed at 200 hPa. It is readily seen that the horizontal wind in the future scenario weakens over the tropics along the Intertropical Convergence Zone (ITCZ) which shifts southward during December–February (DJF) and northward during June–August (JJA). In midlatitudes, the horizontal wind speed increases along the storm track regions in both hemispheres (Northern Hemisphere, NH and Southern Hemisphere, SH) in general for all four seasons. Also, at higher latitudes of the North Atlantic flight corridor (50°N–75°N) which is close to Greenland, the horizontal wind increases in general except for DJF.

Global distribution of aviation turbulence at cruising altitude

The horizontal distributions of the 45-year DJF at 200 hPa of averaged Ellrod1, MWT1, and CGWD, as an example of CAT, MWT, and NCT diagnostics, respectively (Fig. 2a and description in Table 1), clearly show different features spatially. The Ellrod1 indicates relatively strong turbulence along the midlatitude jets, while the MWT1 is strong over the steeper mountains. As expected, the CGWD is strongest over the tropics along the ITCZ which shifts toward the SH during DJF and moves toward the NH during JJA (Supplementary Fig. 1a).

Compared to the historical results, there is an intensification in the Ellrod1 CAT diagnostic over midlatitudes in the SSP5-8.5 results, but weakening over the tropics where both the vertical wind shear and flow deformation are reduced, which is consistent with previous results²⁹. For the MWT1 diagnostic, there are locally intensified areas over most of the mountainous regions under the high-emissions scenario identified from significant increases at the 95% confidence level (see Methods) in the magnitude of turbulence (the middle and lowest panel of Fig. 2a). Given that the MWT indices including the MWT1 used in this study are proportional to CAT indices (Table 1) and the near-surface wind speed in the high mountainous regions (see Methods), the increases in turbulence intensity of the CAT indices and/or the near-surface wind in the climate change scenario could lead to higher MWT1 potential. In the SSP5-8.5 results, the CGWD shows intensification over convective prone regions including the tropics and some of the SH subtropics over the ocean where the column-maximum convective heating rate and convective gravity wave momentum flux at the cloud top are enhanced compared to those in the historical period (Supplementary Fig. 1a).

The same analysis is conducted using the 45-year JJA averaged Ellrod1, MWT1, and CGWD at 200 hPa (Fig. 2b). In JJA of the high-emissions experiment, enhanced vertical wind shear, which is related to strengthened meridional temperature gradient through the thermal wind relation, significantly enhances Ellrod1 along the subtropical jet stream in the SH at the 95% confidence level. As in

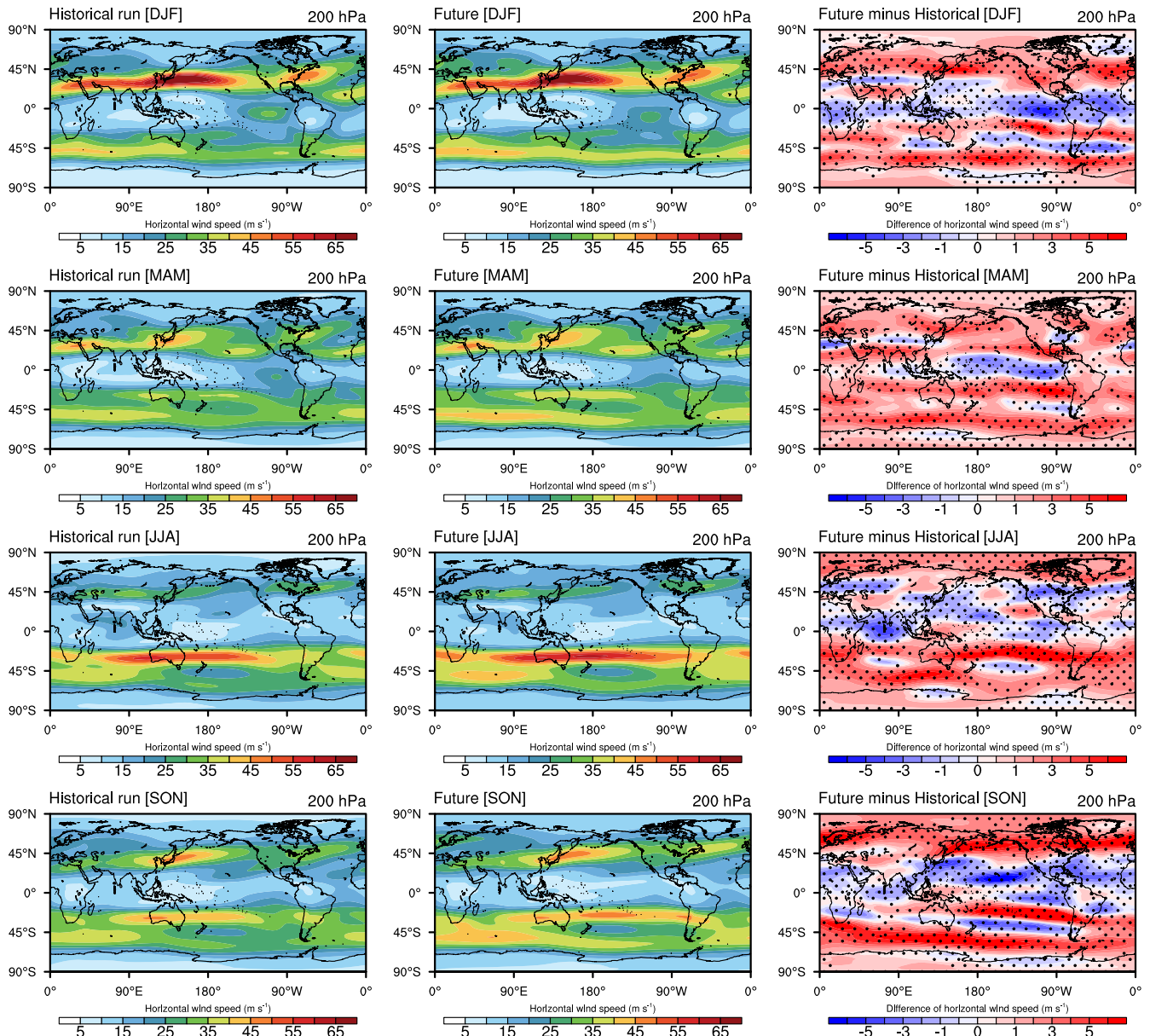


Fig. 1 Upper-level horizontal wind speed predicted from historical and SSP5-8.5 experiments. The 45-year averaged horizontal wind speeds at 200 hPa for DJF (December–February), MAM (March–May), JJA (June–August), and SON (September–November). The leftmost and middle panels show the historical and SSP5-8.5 simulations, respectively. The rightmost panel shows the wind change inferred from SSP5-8.5 minus historical simulations. In the rightmost panel, red shading indicates that the wind speed in the future period (2056–2100) is greater than that in the historical period (1970–2014). Regions with significant differences at the 95% confidence level are stippled.

DJF (Fig. 2a), the magnitude of the Ellrod1 CAT diagnostic over the tropics in JJA decreases due to a weakening of the vertical wind shear in the future scenario. For the MWT1 which is a combination of near-surface wind, terrain height, and CAT index (vertical velocity squared divided by gradient Richardson number, w^2/Ri of Table 1), the future scenario experiment shows strengthening of the MWT1 in midlatitudes, although in some regions the MWT1 decreases due to the weakening in the near surface winds over terrains. The CGWD is concentrated in the tropics and the NH subtropics due to monsoon-related convection. The future projection indicates that CGWD is enhanced over some regions of the tropical Pacific Ocean, Africa, and the NH subtropics including the Gulf of Mexico, and is related to the enhancement of convective heating rate (Supplementary Fig. 1b).

Changes in occurrence of moderate-or-greater-intensity turbulence under high-emission scenario

To quantify the changes in higher intensity level turbulence occurrences, we first calculate the 98th percentile of the probability distributions of each turbulence diagnostic for the historical period and use it as a threshold for moderate-or-greater (MOG) intensity turbulence^{33–35}. Then, using the threshold for each turbulence diagnostic, we compute how often each turbulence diagnostic exceeds the threshold in both the historical period and future period (see Methods). Figure 3 shows the 45-year DJF and JJA averaged occurrence frequency of MOG-level turbulence of Ellrod1, MWT1, and CGWD at 200 hPa. For both DJF and JJA, there is an increase of up to 10.5% in a relative difference (an average of 2%) in the NH and SH midlatitudes frequencies,

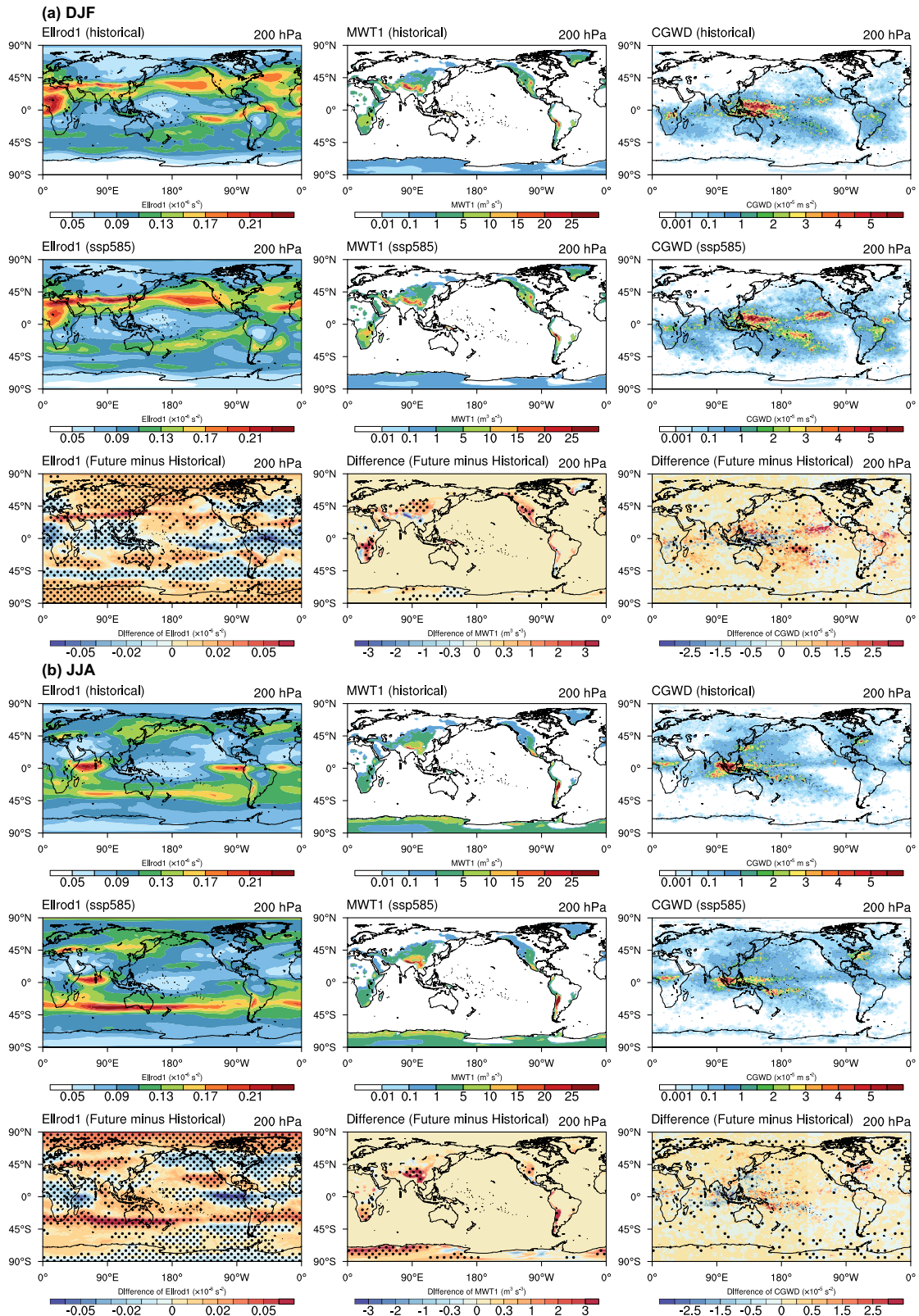


Fig. 2 Global distribution of DJF and JJA aviation turbulence indicators at a typical cruising altitude under the specified climate change scenario. The 45-year averaged selected turbulence diagnostics at 200 hPa for (a) DJF and (b) JJA averaged CAT (Ellrod1), MWT (MWT1), and NCT (CGWD). In a, b, the uppermost and the middle panel show results from the historical simulation and high-emissions simulation, respectively. The lowest panel shows the difference in the magnitudes of each turbulence diagnostic inferred from SSP5-8.5 simulation minus historical simulation. Stippling in the lowest panel indicates the significant difference at the 95% confidence level. Note that CGWD is directly obtained from the CGWD parameterization indicating the wave-breaking regions.

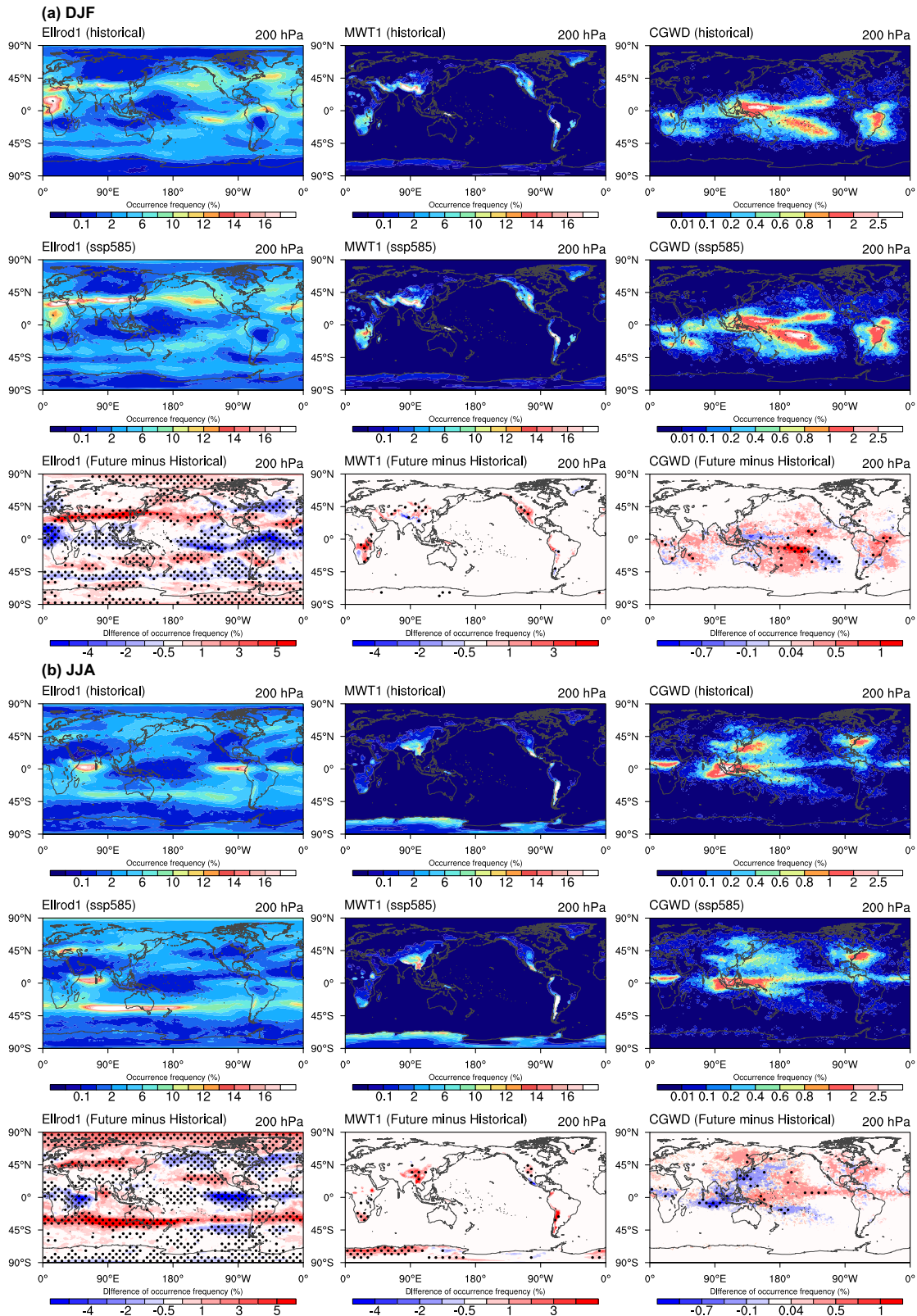


Fig. 3 Global distribution of DJF and JJA occurrence frequencies of aviation turbulence indicators at the typical cruising altitude under the specified climate change scenario. As in Fig. 2, but for the occurrence frequency of MOG-intensity turbulence for 45-year (a) DJF and (b) JJA.

respectively where the upper-level jets are collocated with the regions of the maximum frequency of the Ellrod1.

When focusing on the North Atlantic flight corridor (10°W–60°W and 30°N–75°N), which is the busiest international flight corridor

in the world^{36–38}, during DJF (Fig. 3a), a band of strong Ellrod1 index is revealed over about 40°N–50°N, which was also seen in some previous studies based on reanalysis data³⁹ and climate model simulations³¹. Under the high-emissions scenario, the

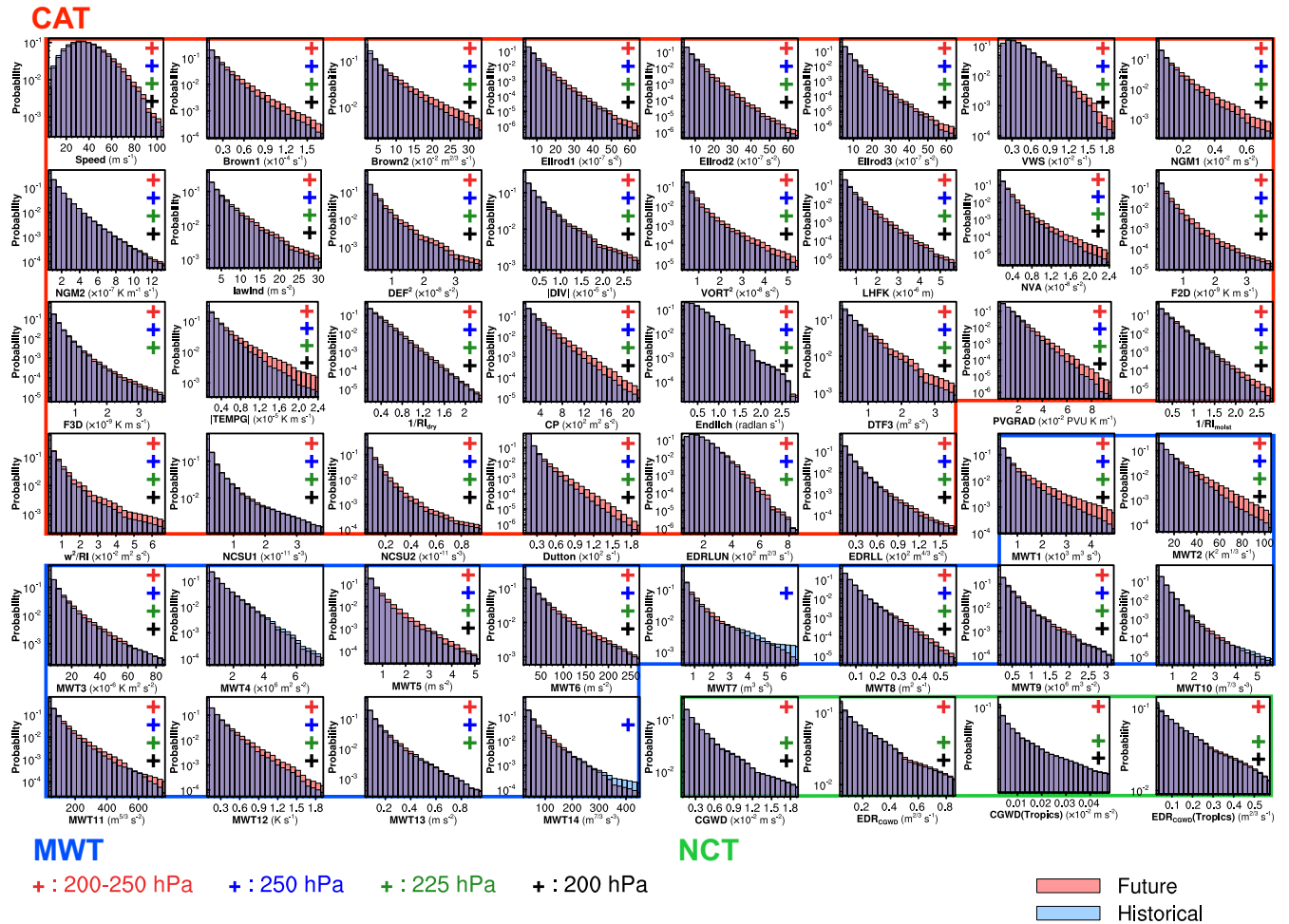


Fig. 4 Probability distributions of upper-level aviation turbulence (CAT, MWT, and NCT) diagnostics under the specified climate change scenario. The probabilities for the 46 turbulence diagnostics used are computed from 45 years of daily-mean data from January to December between 200 and 250 hPa and within extratropics (25°N–65°N and 25°S–65°S). The probabilities of NCT diagnostics are also computed over the tropics (between 25°N and 25°S) and are shown in the bottom-right corner. The blue bar indicates the historical simulation distribution and the red bar indicates the climate change simulation distribution with the specified high-emissions scenario. The overlapped areas are indicated in violet. The plus sign is included when the 98th percentile of the turbulence diagnostic in the future period is greater than that in the historical period. The color of the plus sign indicates the vertical level of data used (red plus: 200–250 hPa, blue plus: 250 hPa, green plus: 225 hPa, and black plus: 200 hPa). The order of turbulence diagnostics used is the same in Table 1.

occurrence frequency of CAT diagnosed by the Ellrod1 index is reduced in this latitude band where both flow deformation and vertical wind shear are decreased. In higher latitudes of the North Atlantic flight corridor (50°N–75°N), the Ellrod1 index is slightly strengthened, due to the cancellation between strongly enhanced flow deformation and less weakened vertical wind shear. Also, the Ellrod1 index in the DJF (Fig. 3a) and JJA (Fig. 3b) in the future climate experiments is weakened, and its occurrence is reduced over the tropics where the horizontal wind speed decreases together with weakened flow deformation and vertical wind shear.

For MWT, the MWT1 diagnostic shows overall increases under the high-emissions scenario except for some areas close to the edges of the Himalayas and Greenland where both the near-surface mountain stress term including near-surface wind and the CAT-related term (w^2/Ri) are decreased for DJF in the future (Fig. 3a). Also, for JJA (Fig. 3b), the MWT1 increases in general except for the southern Sierra Madre Occidental in Mexico where both w^2/Ri and the near-surface wind speed are weakened in the future experiment.

In contrast to the Ellrod1 CAT diagnostic, the CGWD NCT diagnostic occurs more frequently under the high-emissions

scenario in the tropics and SH subtropics in DJF compared to the historical simulation (Fig. 3a). Also, the CGWD during the future period strengthens over some regions of the tropics and NH subtropics in JJA when the maximum convective heating is located in the NH (Fig. 3b and Supplementary Fig. 1b). Note that the CGWD is generally proportional to the magnitude of cloud-top momentum flux of convective gravity waves that is proportional to the square of the diabatic heating rate, and therefore, if convective activity becomes stronger, there can be a greater chance for convective gravity wave breaking at aircraft cruising altitudes in the UTLS.

In addition to the turbulence indices shown in Figs. 2, 3, the entire set of 46 turbulence indices (listed in Table 1) is computed using the 45-year daily-mean outputs from both historical and SSP5-8.5 simulations and is shown as turbulence intensity histograms in Fig. 4 for the extratropics (25°N–65°N and 25°S–65°S) and for three vertical levels of typical aircraft cruising altitudes (200, 225, and 250 hPa). For the NCT diagnostics, the probability distribution over the tropical region between 25°N and 25°S is also shown in the bottom-right corner of Fig. 4. The histograms of most CAT, MWT, and NCT diagnostics in both periods are positively skewed and unimodal. The probability of

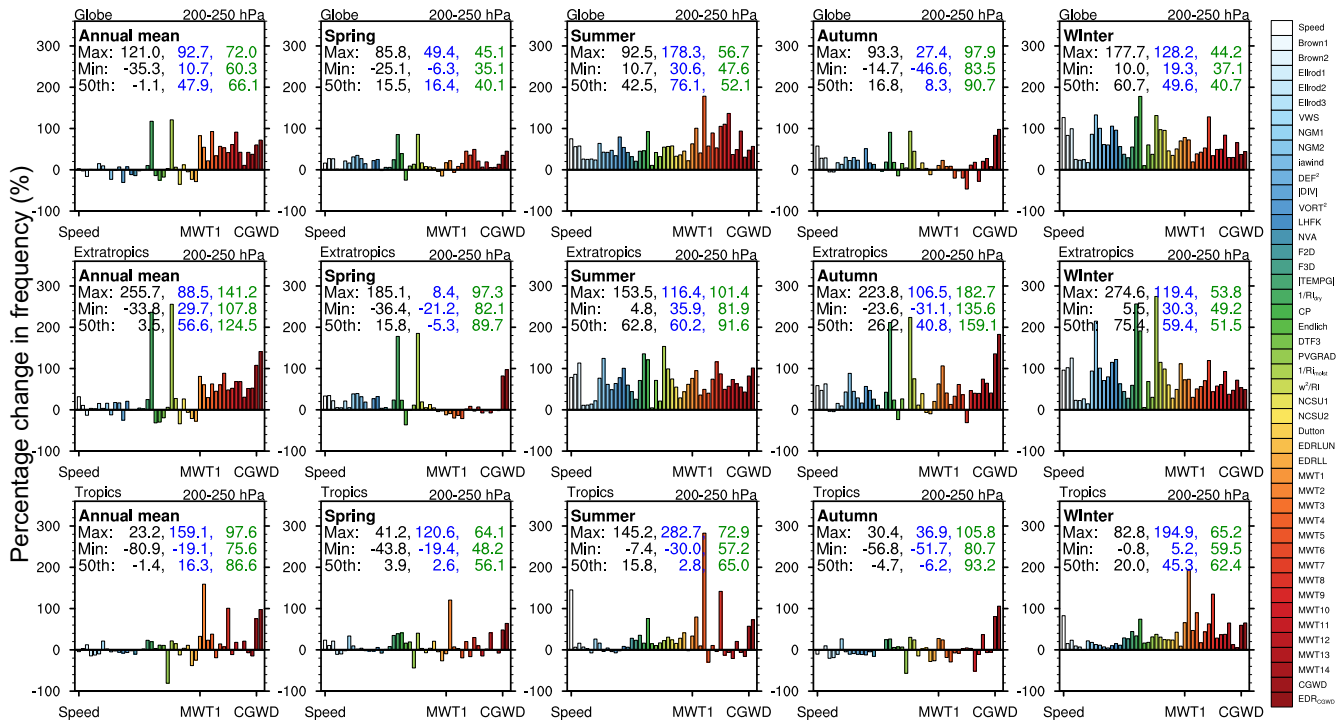


Fig. 5 Percentage increase in the frequency of upper-level aviation turbulence (CAT, MWT, and NCT) under the specified climate change scenario. The bar charts show the percentage change of MOG turbulence diagnosed by the 30 CAT, 14 MWT, and 2 NCT indices between 200 and 250 hPa for the 45-year future period compared to the historical period. The uppermost, middle, and lowest panels are for the global, extratropics, and tropics regions, respectively. The maximum, minimum, and median estimates between each type of turbulence are written in each figure (black: CAT, blue: MWT, and green: NCT). The order of turbulence diagnostics used is the same as in Table 1.

most turbulence diagnostics shifts to the right in the high-emissions scenario projected to the future climate, meaning that there is increased probability of encountering strong turbulence (91% among all turbulence indices). We repeat the same analysis for a single vertical level and put a plus sign (black: 200 hPa, green: 225 hPa, and blue: 250 hPa) in the top-right corner of each plot when the 98th percentile of each turbulence diagnostic in the future period (2056–2100) is greater than that in the historical period (1970–2014). For most of the turbulence indices at the selected vertical levels of 200, 225, and 250 hPa, increased probabilities at strong turbulence intensities appear (by 85, 91, and 91% among all turbulence indices for 200, 225, and 250 hPa, respectively) under the high-emissions scenario.

It is found that the NCT diagnostics are enhanced at three altitude ranges (200–250 hPa, 200 hPa, and 225 hPa) in the future for both extratropics and tropics. However, the NCT at 250 hPa shows decreased probabilities at stronger turbulence intensities, and this is likely associated with an increase in cloud height and a corresponding increase in wave-breaking height in the climate change experiments. Also, most MWT diagnostics are enhanced at three altitude ranges (200, 225, and 250 hPa) under the specified climate change scenario, although some MWT diagnostics (e.g., MWT4, MWT10) exhibit a decrease in probabilities of encountering strong turbulence. Consistent results are obtained from the global probability distributions of turbulence diagnostics (not shown).

Considering that the probabilities of most turbulence diagnostics shift to the right in the high-emission experiment, the current results indicate that the increase is not specific to a certain threshold, but rather to an increase in overall intensity. Therefore, the occurrence frequencies of the 46 turbulence diagnostics are calculated using the 98th percentile and this percentile is applied to all forms of turbulence (CAT, MWT, and NCT) over the globe. This threshold differs from some other previous studies (e.g., 95th, 98th, and 99.6th percentile) to define MOG-level turbulence^{11,28–31,35,40,41}.

As there are uncertainties in the percentile value that defines MOG-level turbulence in the real atmosphere, we have chosen one specific percentile (98th percentile) for the MOG intensity as a tuning factor from the model perspective. When we compute the occurrence frequency of each turbulence diagnostic with three different criteria (the 95th, 98th, and 99.6th percentiles) for MOG-level turbulence, it is found that the changes in the future scenario increase as the criterion increases from the 95th to 99.6th for CAT and MWT, although this was not found in NCT. For the changes in the individual diagnostics, larger variations are found over the extratropics compared to the tropics in higher criterion (99.6th) especially in winter, although the patterns are the same (Supplementary Fig. 2). Therefore, it is found that consistent results are obtained using different percentile thresholds (different intensity levels), although there is a minor discrepancy in the magnitude of the percentage change, at least in the current analysis.

Next, we assess the percentage changes in MOG-level turbulence occurrence for all CAT, MWT, and NCT diagnostics (total of 46 indices) (see Methods). The changes in annual and seasonal means of each diagnostic between 200 and 250 hPa for 45 years are computed over the globe, extratropics, and tropics separately (Fig. 5). Over the globe (the uppermost panel of Fig. 5), more than half of the CAT, MWT, and NCT diagnostics show positive changes by 8–91% in the median estimates and by 27–178% in the maximum estimates, indicating that turbulence is intensified overall compared to the historical experiments. This increasing result is consistent to some previous results on CAT^{29,31,42}.

For seasonal mean percentage changes over the globe, most CAT, MWT, and NCT diagnostics intensify in the high-emissions scenario (more than 36 indices for each season). All 46 turbulence diagnostics show an increase in the frequency of occurrence in the climate change experiment for both summer and winter with positive percentage changes up to 76% (summer) and 61% (winter) in the median estimates. The NCT indices show greater

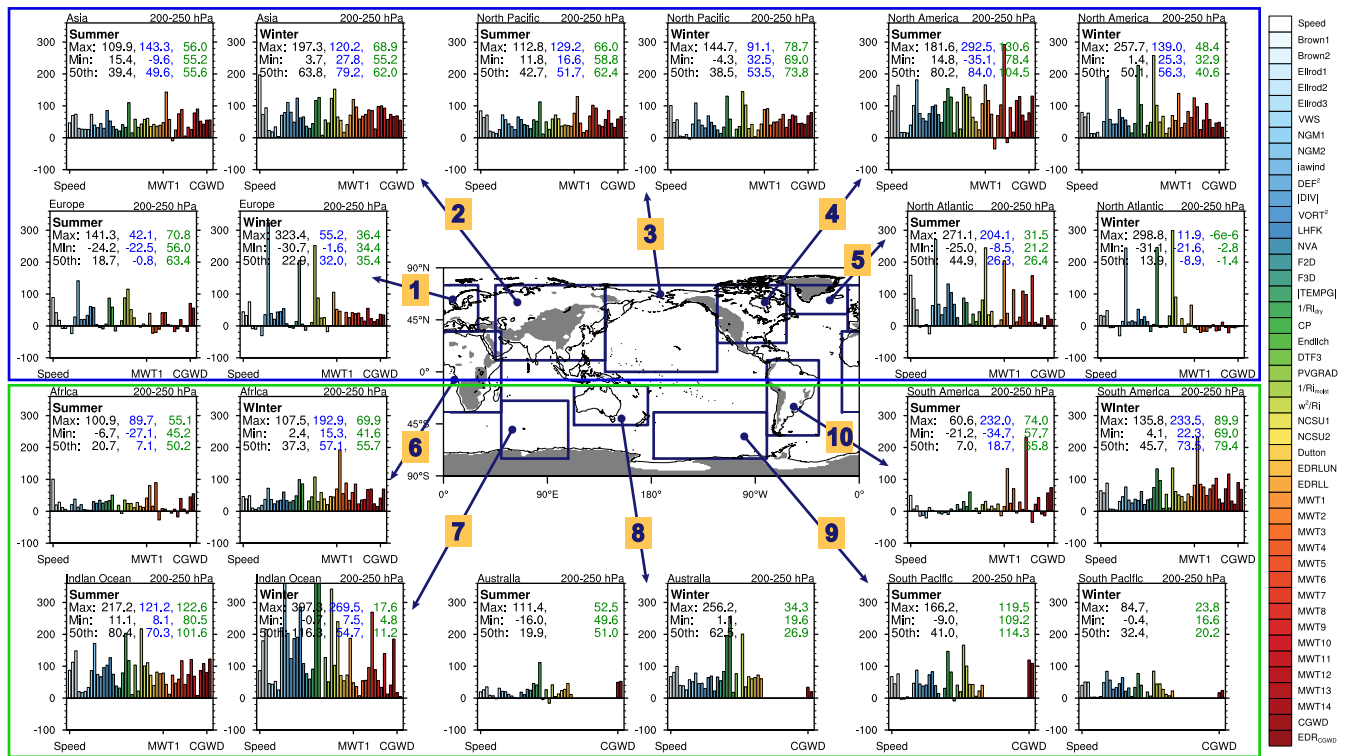


Fig. 6 Response of upper-level aviation turbulence (CAT, MWT, and NCT) under the specified climate change scenario over ten specified regions. The bar charts show the percentage change of occurrence frequency of MOG turbulence between 200 and 250 hPa in summer and winter for 45 years. The histograms are calculated using the data within each box with arrows and labels. The maximum, minimum, and median estimates between each type of turbulence are written in each figure (black: CAT, blue: MWT, and green: NCT). The order of turbulence diagnostics used is the same as in Table 1 and Fig. 5. The gray shaded areas indicate MWT prone regions.

increase in the occurrence frequency in summer than in winter, compared to the historical experiment (e.g., 57 and 44% increases by EDR_{CGWD} in summer and winter, respectively). Also, enhancements in convective activity over the tropics and NH and SH subtropics (for SON and MAM, respectively) were found in both NH and SH autumn (not shown), and correspondingly, NCT indices increase by up to 91% in the median estimates in autumn. Therefore, while some indices show a decrease in future turbulence occurrence, overall increases in turbulence occurrence can be found from a perspective of an ensemble of turbulence indices for all three forms of turbulence (CAT, MWT, and NCT).

Regionally (two lower panels of Fig. 5), at least two thirds of turbulence indices (more than 29 indices) indicate positive percentage changes under a changing climate, except for the autumn over the tropics where negative percentage changes occur for 16 and 8 indices of CAT and MWT, respectively, likely related to significantly weaker horizontal wind speed at the 95% confidence level in the future period (the rightmost panel of Fig. 1). Extratropical variations in the percentage change are much larger (16–159% increase of seasonal median estimates) than over the tropics (3–93% increase of seasonal median estimates). In the extratropics where upper-level jets are located and most mountains exist, regional changes in the occurrence frequency of CAT and MWT are greater in summer and winter than in spring and autumn in both hemispheres. In both summer and winter, all turbulence indices consistently show extratropical enhancement in future turbulence intensity and occurrence frequency compared to the historical period. In the tropics, small changes (or negative values) in occurrence frequency of MOG-level turbulence are revealed in general, although MWT2 and MWT4 dramatically increase in winter and summer, respectively. NCT indices, which diagnose more localized turbulence compared to other CAT and

MWT indices²⁷, show turbulence enhancements over the tropics and extratropics for all seasons.

As mentioned above, we additionally computed the percentage change of the occurrence frequency of turbulence using three different MOG-level threshold values (95th, 98th, and 99.6th percentile). Regardless of the MOG threshold used, we found similar increases in occurrence frequencies in general, with larger variations over the extratropics compared to the tropics (Supplementary Fig. 2) when using the higher (99.6th) percentile. That is, consistent results are obtained using different percentile thresholds (different intensity levels) for all types of turbulence (CAT, MWT, and NCT), although there is a difference in the magnitude of the percentage change, at least in the current analysis. Also, it is noteworthy that the MOG-level turbulence threshold is calculated from the probability distribution without considering area weights. When we compute percentage changes in frequency of MOG-level turbulence occurrence using the threshold obtained from area-weighted probability distribution, consistent results of increase in turbulence occurrence are obtained over the global, tropical, and extratropical regions, although there are some minor discrepancies in the magnitudes of percentage changes. Future study considering area-weighted probability distributions should be conducted to account for the convergence of meridians and corresponding reduction in grid cell areas towards the pole, which reduces the possible over-representations of the MOG-level turbulence frequencies in higher latitudes.

We find a commonality among the global, tropical, and extratropical regions that shows remarkable changes in summer and winter compared to other seasons (Fig. 5). Taking this into account, to examine the characteristics in changes of turbulence occurrence due to climate change locally, we subdivided the globe into ten specific regions (see Methods and boxes of Fig. 6). For these regions, the percentage changes in MOG-level

turbulence occurrence between 200 and 250 hPa in summer and winter for 45 years are quantified as indicated in Fig. 6. Note that when a turbulence diagnostic does not exceed the 98th percentile threshold for the historical period, its percentage change is set to missing (as for MWT8 in region 6) in the present study.

For the busiest international airspace in the middle and high latitudes of the NH (regions 1–5)²⁹, the ensemble of turbulence diagnostics shows increases of 19–80% (14–64%) in the median estimates for the CAT, 26–84% (32–79%) in those for the MWT, and 26–105% (35–74%) in those for the NCT under the SSP5-8.5 simulations for summer (winter). The NCT diagnostics show decreases over the North Atlantic (region 5) for winter, which may be related to weakened convective heating (Supplementary Fig. 1). Although the magnitude of the CAT changes is relatively small compared to previous studies^{29–31}, the trend is the same, i.e., the CAT diagnostics show increases in MOG turbulence occurrence. When we conduct the same analysis using the 99.6th percentile used as the threshold of MOG-level turbulence in previous studies^{29–31}, consistently, there is an increase in the frequency of MOG-level CAT occurrences (not shown). This difference could also be related to different settings (such as model configurations) of the climate models used. Nevertheless, our results consistently show future turbulence intensification and increase in the occurrence frequency of CAT. In the analyses of MWT and NCT changes, we found overall positive median increases in the busiest international airspaces (regions 1–5, except MWT in region 1 for summer and MWT and NCT in region 5 for winter), meaning increases in turbulence occurrence.

However, there are regions indicating decreases by some turbulence diagnostics in turbulence occurrence in the future period. In region 1 (Europe) in the summertime, six MWT diagnostics (MWT3, MWT4, MWT5, MWT10, MWT11, and MWT14) show negative percentage changes of up to –23%. Also, in region 5 (North Atlantic Ocean) in the wintertime, 12 MWT diagnostics except for MWT7 and MWT10 show decreases in the occurrence frequency of turbulence (up to –22%). This may be associated with the weakened near-surface wind speed and/or CAT diagnostics, however, it is quite complicated to clearly explain why there are increases or decreases in MWT intensity and occurrence frequency, as not only near-surface condition but also upper-level background condition favorable to mountain wave breaking are relevant to MWT. Also in region 5, the NCT diagnostics show decreased occurrence frequency in the future wintertime, which may be associated with weakened convective heating rates and cloud top momentum flux of convective gravity waves (as shown in Supplementary Fig. 1a) and also background conditions such as wind and static stability over this region.

For less congested airspace regions such as over Africa and South America, we conducted the same analysis for the 45-year summer and winter seasons. As the MWT diagnostics are activated only in mountainous regions, some regions (regions 8 and 9) do not have MWT estimates. In regions 6 and 8–10, turbulence diagnostics show positive percentage changes in the median estimates with 7–41% (32–63%) for CAT, 7–19% (57–74%) for MWT, and 50–114% (20–79%) for NCT under the SSP5-8.5 experiments for summer (winter), which is consistent to results in regions 1–5. Especially, over the Indian Ocean (region 7) where significantly enhanced winds are expected under the SSP5-8.5 scenario (Fig. 1), turbulence increases greatly especially for CAT (80 and 116% in the median estimates for summer and winter, respectively). This aspect needs further modeling/observational studies in the future. In region 10 (South America), some CAT diagnostics that are mostly related to the shear instability (9 CAT diagnostics) estimate decreases in summertime turbulence occurrence for the future period (up to –21%). Although expected regional percentage changes vary for each type of turbulence, in terms of the median estimates (the ensemble of turbulence

diagnostics) for all types of turbulence, aircraft can expect to experience a much bumpier flight in a changing climate.

DISCUSSION

This study examined changes in the intensity of aviation turbulence and occurrence of the MOG-level turbulence at typical cruising altitudes in the future using long-term climate model data from historical and high-emission experiments. As the characteristics of free atmosphere turbulence depend strongly on its source, considering future changes of intensity and occurrence frequency for all three types of turbulence, not exclusively for CAT considered in some previous studies, are required. Therefore, turbulence generated from three sources, CAT, as well as MWT and NCT was considered.

The current results demonstrate that all three types of turbulence (CAT, MWT, and NCT) will strengthen in most regions globally for all seasons as a response to climate change (globally seasonal increase up to 91% in the median estimates), except that CAT and MWT are weakened for autumn in the tropics. At typical aircraft cruising altitudes in the UTLS for ten specified regions, most turbulence diagnostics show 7–80%, 7–84%, and 26–114% (14–116%, 32–79%, and 11–79%) increases in the median estimates of the occurrence frequency of MOG-level CAT, MWT, and NCT, respectively, for summer (winter) seasons under the changed climate compared to the historical experiments. The current results are consistent with previous studies^{38,39,42} for CAT using long-term reanalysis and climate model data that have suggested an increasing trend of flight bumpiness. Although the climate model data and turbulence diagnostics used in this study are different or partially overlap those used in some previous studies, we obtain consistent results on the CAT responses to the future climate conditions with those studies, bolstering confidence in this key result. Like CAT, most MWT and NCT indices showed increases in turbulence occurrence in the changed climate scenario.

Assuming flight tracks are fixed, these results imply that we can expect that climate change will cause bumpier flights with respect to all possible types of upper-level turbulence. In this regard, flight routing may become more complicated to avoid and detour around turbulent air, and this may cause extended flight times⁴³ and increased fuel consumption and emissions from commercial aircraft. This in turn, may provide positive feedback, whereby these additional emissions could actually accelerate global warming.

There are several limitations and future considerations related to the current study. Regarding spatiotemporal resolution of climate model data, the spatial grids are still too coarse to explicitly capture turbulence at aviation scales. Also, the lower temporal resolution (e.g., 1 day) of climate models may have limitations in capturing the intermittent nature of some forcing mechanisms and the consequent turbulence. Although a previous study used 6-hourly outputs²⁹ to compute CAT response, it is currently not possible to examine the future response of all forms of turbulence (CAT, MWT, and NCT) as some meteorological variables are not available (e.g., relative humidity and cloud ice and water mixing ratio) at the 6-hourly temporal resolution. To make sure the consistency between the daily-mean versus 6-hourly data, we compared the 6-hourly outputs for the four variables (zonal and meridional wind, air temperature, and geopotential height) with daily mean data that both are available for the NorESM2-MM for 45 years of the climate change scenario. Also, from two datasets, the Ellrod1 index is calculated. When the horizontal distributions and probability distributions of 6-hourly based data are compared to those derived from the daily-mean data, we found that the 6-hourly and daily-mean results have similar distributions, although the magnitude of the 6-hourly outputs is larger than that of the daily-mean outputs

(Supplementary Figs. 3, 4). If the model variables for which the CAT, MWT, and NCT diagnostics can be calculated are available with a better temporal resolution, further analysis should be conducted in the future study.

Further, as this study has considered the extreme emission scenario only, the dependency on other climate change scenarios and climate models needs to be conducted in the future. In addition to uncertainties associated with the climate models/scenarios used, there are also uncertainties in the turbulence diagnostics. Further analysis using model data with better spatiotemporal resolution and their effects on model-based turbulence diagnosis is required to better quantify these uncertainties.

METHODS

Data

The NorESM2-MM data were generated as a part of the Coupled Model Intercomparison Project Phase 6 (CMIP6). We archived 45-years (historical: 1970–2014 and SSP5-8.5: 2056–2100) of daily-mean NorESM2-MM datasets with a 1.25° in longitude by 0.94° in latitude, having 288×192 grid points. This is finer than the spatial resolution used in previous studies using climate model data^{29,31}. The simulated results have 32 layers in a hybrid sigma-pressure coordinate and these are interpolated to 25-hPa spacing. Here, we used three interpolated pressure levels between 200 and 250 hPa that are close to typical cruising altitudes of commercial aircraft. Second-order centered finite differences are used to approximate horizontal and vertical derivatives throughout.

To choose the model for our analysis within the CMIP6 suite, we investigated very carefully the evaluation results of several variables provided by the program for climate model diagnostics and intercomparison (PCMDI, https://pcmdi.llnl.gov/research/metrics/mean_clim) and the availability of meteorological variables to calculate the turbulence diagnostics. First, we shortlisted candidates based on the PCMDI spatiotemporal root mean square differences (global-mean 200-hPa wind) against European Centre for Medium-Range Weather Forecasts Re-Analysis, version 5 (ERA-5⁴⁴) reanalysis data. The NorESM2-MM showed top-ranked skills not only for winds but for other variables at different levels. Second, we looked at which models provide all variables to derive all CAT, MWT, and NCT diagnostics used in this study, viz., the zonal, meridional, and vertical wind, air temperature, geopotential height, relative humidity, and cloud ice and water mixing ratio. To the authors' knowledge, the daily-mean NorESM2-MM is the only source that met all requirements, providing a horizontal resolution of $\sim 1^\circ$ and a sufficient number of vertical layers from the surface to the model top. This is the main reason why we use daily-mean data from the NorESM2-MM.

Turbulence diagnostics

The CAT diagnostics are mostly related to shear and inertial instability (top 30 turbulence diagnostics in Table 1)^{18,19}. Also, to compute the MWT diagnostics¹⁹, the near-surface forcing term is used:

$$d_s = 0 \text{ if } h < 700 \text{ m} \quad (1)$$

$$d_s = V_L (\max \text{ in lowest } 1500 \text{ m}) \times \min(h, 2750 \text{ m}) \text{ if } h \geq 700 \text{ m}, \quad (2)$$

where h is terrain height, V_L is the maximum low-level wind speed within 1.5 km of the terrain. The threshold of the terrain height was determined to cover MWT-prone regions such as the Rocky Mountains, the Andes, and the Himalayas. The mountain wave term (d_s) is multiplied by selected CAT diagnostics¹⁹ (see Table 1). The computation of the MWT diagnostics is activated if the terrain height is more than 700 m which is represented as gray shading in Fig. 6.

The NCT diagnostics are based on the CGWD parameterization scheme proposed by Chun and Baik (1998)⁴⁵ which has been

implemented in both climate models and global weather prediction models^{46–49}. The CGWD parameterization is activated only at grid points where convective clouds exist and only above the cloud top. A brief description of the CGWD parameterization is as follows: we first calculate convective gravity wave (CGW) momentum flux at the cloud top, and then the CGW momentum flux at just one level above the cloud top is calculated by checking the minimum Richardson number (Ri_m) which includes the modifying effects of CGWs. If $Ri_m < 1/4$, it is assumed that wave breaking occurs and the saturated CGW momentum flux is calculated, while if $Ri_m \geq 1/4$, the CGW momentum flux at that level is set to the cloud-top momentum flux of CGW⁵⁰. This procedure is repeated until the model top is reached. From the vertical profile of CGW momentum flux, the CGWD is calculated as:

$$\text{CGWD} = |(-1/\rho)(\partial\tau/\partial z)|, \quad (3)$$

where ρ is the air density, τ is the CGW momentum flux.

The CGWD output can be used directly as a NCT diagnostic. In addition, the CGWD can be used to derive a diffusion coefficient using Lindzen's linear wave saturation hypothesis⁵¹ and subsequently the cube root of energy dissipation rate (EDR_{CGWD}) based on a turbulence closure assumption^{27,52,53}:

$$\text{EDR}_{\text{CGWD}} = 10 C_\epsilon^{1/3} |(\text{CGWD}/L^{4/3})(U/N^{-2})|, \quad (4)$$

where C_ϵ is the constant of 0.93, L is the length scale which is set to 100 m^{11,27,54}, U and N are the basic-state wind and static stability projected onto the wind vector at the cloud top, respectively. Finally, NCT is diagnosed from the two estimates CGWD and EDR_{CGWD} .

For the NCT calculation, the convective heating rate information and cloud top and bottom heights are required. The NorESM2-MM does not publicly provide the convective heating rate and cloud top and bottom heights as standard outputs like many global reanalysis and analysis datasets. Because of this, the convective heating rate has to be estimated using water vapor mixing ratio, air temperature, vertical velocity, and relative humidity²⁷. The cloud top and bottom are defined as the altitude where the convective heating rate falls to 20% and 5%, respectively, from the column-maximum convective heating rate at each grid point^{55,56}. To eliminate shallow convective cases, the CGWD and NCT calculations are activated only when the depth of clouds, that is calculated using cloud top and bottom heights, is greater than 1 km.

Even though daily means were used to compute the NCT diagnostics, convection related to large scale forcing such as synoptic fronts would be expected to be fairly well represented by daily means. However, isolated convection over summertime continents and in the tropics may be missed. In the future, if the CGWD output is available as the standard output, the CGWD outputs could be directly utilized as the NCT diagnostic without postprocessing calculations. While further analysis using higher-resolution (both spatial and temporal) climate model data should be conducted in the future, it is considered feasible to calculate the NCT diagnostics and the NCT changes at the current temporal resolution.

This study did not focus on the difference in the number of turbulence diagnostics for each type of turbulence, but rather focus on the possible generation mechanisms of turbulence, which is considered as known sources in this study. Here, the CAT diagnostics used can diagnose turbulence due to various generation mechanisms such as shear and inertial instabilities associated with upper-level jets and fronts. In the same manner, MWT diagnostics used can infer turbulence related to mountain wave breaking and wave-induced triggers combined with CAT diagnostics. And, the NCT diagnostics diagnosing CGW breaking were chosen as a known source for NCT in the analysis. Therefore, the choice of indices for each source of turbulence is not related

to the sample size for each type of turbulence, but rather source-based selection of turbulence diagnostics.

Frequency of turbulence occurrence and percentage change of turbulence occurrence

The 98th percentile of the probability distribution of each turbulence computed between 200 and 250 hPa over the globe is computed for 45 years of the historical period and it is used as the threshold of MOG-level turbulence. The occurrence frequency of turbulence is computed using this MOG-level threshold for both the historical and future periods. That is, if a turbulence diagnostic exceeds the 98th percentile, we classified it as the MOG-level turbulence. This same criteria of MOG-level turbulence is applied to all CAT, MWT, and NCT diagnostics. If the area-weighting is applied to compute probability distribution, we did not find noticeable difference in the occurrence frequency of turbulence between probability distributions with and without area weightings (not shown).

The percentage change of turbulence occurrence is calculated as:

$$\alpha[\%] = \frac{\text{frequency}_{SSP5-8.5} - \text{frequency}_{\text{historical}}}{\text{frequency}_{\text{historical}}} \times 100, \quad (5)$$

Where α is the percentage change in occurrence frequency in units of % and $\text{frequency}_{SSP5-8.5}$ and $\text{frequency}_{\text{historical}}$ indicate the frequencies of MOG turbulence using the outputs of the SSP5-8.5 and historical simulations, respectively. This measure of turbulence change under a changing climate was used in other previous studies^{28–31,42,57}. As the percentage change calculated from Eq. (5) is a relative value, the negative percentage change indicates decreases in turbulence occurrence in the future period compared to the historical period.

To examine regional percentage changes in the occurrence frequency of the MOG-level turbulence, ten regions (boxes of Fig. 6) are specified as follows: 35°N–75°N, 10°W–30°E (1. Europe); 10°N–75°N, 45°E–140°E (2. Asia); 0°N–75°N, 123°W–140°E (3. North Pacific); 25°N–75°N, 63°W–123°W (4. North America); 50°N–75°N, 10°W–60°W (5. North Atlantic); 15°S–50°N, 35°W–35°E (6. Africa); 25°S–75°S, 50°E–108°E (7. Indian Ocean); 12°S–46°S, 113°E–177°E (8. Australia); 35°S–75°S, 80°W–178°W (9. South Pacific); 55°S–10°N, 35°W–80°W (10. South America). Regions 1, 2, 4–6, 8, and 10 are the same as used in a previous study²⁹, while two additional sub-regions (Regions 7 and 9) are selected considering a horizontal distribution of reported number of aircraft-based observations over the globe⁵⁸, and Region 3 is set to cover most of the North Pacific Ocean. For the ten specified regions, the median and maximum estimates of percentage change of occurrence frequency of MOG-level turbulence are computed for each turbulence source.

Significance test

The significance test on differences of horizontal wind speed, turbulence diagnostics, and occurrence frequencies of turbulence between the historical period and future period are conducted at the 95% confidence levels (p -value < 0.05, $n = 45$) with a two-sided t-test. Here, n is the sample size. Areas satisfying this significance test are shown as stippled regions in Figs. 1–3.

DATA AVAILABILITY

All figures in this manuscript use the CMIP6 NorESM2-MM data available at <https://esgf-node.llnl.gov/search/cmip6>. The DOIs of the NorESM2-MM datasets are <https://doi.org/10.22033/ESGF/CMIP6.8040> (historical) and <https://doi.org/10.22033/ESGF/CMIP6.8321> (SSP5-8.5).

CODE AVAILABILITY

The codes supporting the findings of this study are developed by the corresponding authors and available on reasonable request.

Received: 21 December 2022; Accepted: 4 July 2023;

Published online: 14 July 2023

REFERENCES

1. Sharman, R. D. & Lane, T. P. Lane. *Aviation Turbulence: Process, Detection, Prediction* 1st edn (Springer, 2016).
2. Gultepe, I. et al. A review of high impact weather for aviation meteorology. *Pure Appl. Geophys.* **176**, 1869–1921 (2019).
3. Lester, P. F. *Turbulence: A New Perspective for Pilots* 1st edn (Jeppesen Sanderson, 1994).
4. Kim, J.-H. et al. Improvements in nonconvective aviation turbulence prediction for the World Area Forecast System. *Bull. Am. Meteorol. Soc.* **99**, 2295–2311 (2018).
5. Dutton, J. A. & Panofsky, H. A. Clear air turbulence: a mystery may be unfolding. *Science* **167**, 937–944 (1970).
6. Zhang, F. Generation of mesoscale gravity waves in upper-tropospheric jet-front systems. *J. Atmos. Sci.* **61**, 440–457 (2004).
7. Doyle, J. D., Shapiro, M. A., Jiang, Q. & Bartels, D. L. Large-amplitude mountain wave breaking over Greenland. *J. Atmos. Sci.* **62**, 3106–3126 (2005).
8. Sharman, R. D. & Trier, S. B. Influences of gravity waves on convectively induced turbulence (CIT): A review. *Pure Appl. Geophys.* **176**, 1923–1958 (2019).
9. Lane, T. P. & Sharman, R. D. Some influences of background flow conditions on the generation of turbulence due to gravity wave breaking above deep convection. *J. Appl. Meteorol. Climatol.* **47**, 2777–2796 (2008).
10. Kim, J.-H. & Chun, H.-Y. A numerical simulation of convectively induced turbulence above deep convection. *J. Appl. Meteorol. Climatol.* **51**, 118–1200 (2012).
11. Kim, S.-H., Chun, H.-Y., Sharman, R. D. & Trier, S. B. Development of near-cloud turbulence diagnostics based on a convective gravity wave drag parameterization. *J. Appl. Meteorol. Climatol.* **58**, 1725–1750 (2019).
12. Kim, J.-H., Chun, H.-Y., Sharman, R. D. & Trier, S. B. The role of vertical shear on aviation turbulence within cirrus bands of a simulated western Pacific cyclone. *Mon. Weather Rev.* **142**, 2794–2813 (2014).
13. Lane, T. P., Sharman, R. D., Clark, T. L. & Hsu, H.-M. An investigation of turbulence generation mechanisms above deep convection. *J. Atmos. Sci.* **60**, 1297–1321 (2003).
14. Lane, T. P. et al. Recent advances in the understanding of near-cloud turbulence. *Bull. Am. Meteorol. Soc.* **93**, 499–515 (2012).
15. Trier, S. B. & Sharman, R. D. Convection-permitting simulations of the environment supporting widespread turbulence within the upper-level outflow of a mesoscale convective system. *Mon. Weather Rev.* **137**, 1972–1990 (2009).
16. Trier, S. B. & Sharman, R. D. Mechanisms influencing cirrus banding and aviation turbulence near a convectively enhanced upper-level jet stream. *Mon. Weather Rev.* **144**, 3003–3027 (2016).
17. Trier, S. B., Sharman, R. D. & Lane, T. P. Influences of moist convection on a cold-season outbreak of clear-air turbulence (CAT). *Mon. Weather Rev.* **140**, 2477–2496 (2012).
18. Sharman, R. D., Tebaldi, C., Wiener, G. & Wolff, J. An integrated approach to mid- and upper-level turbulence forecasting. *Weather Forecast.* **21**, 268–287 (2006).
19. Sharman, R. D. & Pearson, J. Prediction of energy dissipation rates for aviation turbulence. Part I: Forecasting nonconvective turbulence. *J. Appl. Meteorol. Climatol.* **56**, 317–337 (2017).
20. Kim, S.-H. & Chun, H.-Y. Aviation turbulence encounters detected from aircraft observations: spatiotemporal characteristics and application to Korean Aviation Turbulence Guidance. *Meteorol. Appl.* **23**, 594–604 (2016).
21. Cho, J. Y. N. & Linborg, E. Horizontal velocity structure functions in the upper troposphere and lower stratosphere: 1. Observations. *J. Geophys. Res.* **106**, 10223–10232 (2001).
22. Pearson, J. & Sharman, R. D. Prediction of energy dissipation rates for aviation turbulence. Part II: Nowcasting convective and nonconvective turbulence. *J. Appl. Meteorol. Climatol.* **56**, 339–351 (2017).
23. Lee, D.-B. & Chun, H.-Y. Development of the Global-Korean aviation Turbulence Guidance (Global-KTG) system using the Global Data Assimilation and Prediction System (GDAPS) of the Korea Meteorological Administration (KMA) (in Korean with English abstract). *Atmosphere* **28**, 1–10 (2018).
24. Ellrod, G. P. & Knapp, D. I. An objective clear-air turbulence forecasting technique: Verification and operational use. *Weather Forecast.* **7**, 150–165 (1992).
25. Ellrod, G. P. & Knox, J. A. Improvements to an operational clear-air turbulence diagnostic index by addition of a divergence trend term. *Weather Forecast.* **25**, 789–798 (2010).

26. Brown, R. New indices to locate clear-air turbulence. *Meteorol. Mag.* **102**, 347–361 (1973).
27. Kim, S.-H. et al. Improving numerical weather prediction-based near-cloud aviation turbulence forecasts by diagnosing convective gravity wave breaking. *Weather Forecast.* **36**, 1735–1757 (2021).
28. Atrill, J., Sushama, L. & Teufel, B. Clear-air turbulence in a changing climate and its impact on polar aviation. *Saf. Extrem. Environ.* **3**, 103–124 (2021).
29. Storer, L. N., Williams, P. D. & Joshi, M. M. Global response of clear-air turbulence to climate change. *Geophys. Res. Lett.* **44**, 9976–9984 (2017).
30. Williams, P. D. Increased light, moderate, and severe clear-air turbulence in response to climate change. *Adv. Atmos. Sci.* **34**, 576–586 (2017).
31. Williams, P. D. & Joshi, M. Intensification of winter transatlantic aviation turbulence in response to climate change. *Nat. Clim. Chang.* **3**, 644–648 (2013).
32. Seland, Ø. et al. Overview of the Norwegian Earth System Model (NorESM2) and key climate response of CMIP6 DECK, historical, and scenario simulations. *Geosci. Model Dev.* **13**, 6165–6200 (2020).
33. Wolff, J. K. & Sharman, R. D. Climatology of upper-level turbulence over the contiguous United States. *J. Appl. Meteorol. Climatol.* **47**, 2198–2214 (2008).
34. Sharman, R. D., Cornman, L. B., Meymaris, G. & Pearson, J. Description and derived climatologies of automated in situ eddy-dissipation-rate reports of atmospheric turbulence. *J. Appl. Meteorol. Climatol.* **53**, 1416–1432 (2014).
35. Lee, D. B., Chun, H.-Y. & Kim, J.-H. Evaluation of multimodel-based ensemble forecasts for clear-air turbulence. *Weather Forecast.* **35**, 507–521 (2020).
36. Irvine, E. A. et al. Characterizing North Atlantic weather patterns for climate-optimal aircraft routing. *Meteorol. Appl.* **20**, 80–93 (2013).
37. Lee, S. H., Williams, P. D. & Frame, T. H. A. Increased shear in the North Atlantic upper-level jet stream over the past four decades. *Nature* **572**, 639–642 (2019).
38. Williams, P. D. Transatlantic flight times and climate change. *Environ. Res. Lett.* **11**, 024008 (2016).
39. Jaeger, E. B. & Sprenger, M. A. Northern Hemispheric climatology of indices for clear air turbulence in the tropopause region derived from ERA40 reanalysis data. *J. Geophys. Res.* **112**, D20106 (2007).
40. Kim, J.-H. et al. Impact of the North Atlantic oscillation on transatlantic flight routes and clear-air turbulence. *J. Appl. Meteorol. Climatol.* **55**, 763–771 (2016).
41. Lee, J. H. et al. Climatology of clear-air turbulence in upper troposphere and lower stratosphere in the Northern Hemisphere using ERA5 reanalysis data. *J. Geophys. Res. Atmos.* **128**, e2022JD037679 (2023).
42. Williams, P. D. & Storer, L. N. Can a climate model successfully diagnose clear-air turbulence and its response to climate change? *Q. J. R. Meteorol. Soc.* **148**, 1424–1438 (2022).
43. Kim, J.-H., William, N. C., Sridhar, B. & Sharman, R. D. Combined winds and turbulence prediction system for automated air-traffic management applications. *J. Appl. Meteorol. Climatol.* **54**, 766–784 (2015).
44. Hersbach, H. et al. The ERA5 global reanalysis. *Q. J. R. Meteorol. Soc.* **146**, 1999–2049 (2020).
45. Chun, H.-Y. & Baik, J. J. Momentum flux by thermally induced internal gravity waves and its approximation for large-scale models. *J. Atmos. Sci.* **55**, 3299–3310 (1998).
46. Chun, H.-Y., Song, M.-D., Kim, J.-W. & Baik, J.-J. Effects of gravity wave drag induced by cumulus convection on the atmospheric general circulation. *J. Atmos. Sci.* **58**, 302–319 (2001).
47. Chun, H.-Y., Song, I.-S., Baik, J.-J. & Kim, Y.-J. Impact of a coconvectively forced gravity wave drag parameterization in NCAR CCM3. *J. Clim.* **17**, 3530–3547 (2004).
48. Saha, S. et al. The NCEP climate forecast system version 2. *J. Clim.* **27**, 2185–2208 (2014).
49. Baek, S. A revised radiation package of G-packed McICA and two-stream approximation: performance evaluation in a global weather forecasting model. *J. Adv. Model. Earth Syst.* **9**, 1628–1640 (2017).
50. Eliassen, A. & Palm, E. On the transfer of energy in stationary mountain waves. *Geophys. Publ.* **22**, 1–23 (1961).
51. Lindzen, R. S. Turbulence and stress due to gravity wave and tidal breakdown. *J. Geophys. Res.* **86**, 9707–9714 (1981).
52. Deardorff, J. W. Stratocumulus-capped mixed layers derived from a three-dimensional model. *Bound. Layer. Meteorol.* **18**, 495–527 (1980).
53. Lilly, D. K. On the application of the eddy viscosity concept in the inertial sub-range of turbulence. *NCAR Tech Rep.* **123** (1966).
54. Moeng, C.-H. & Wyngaard, J. C. Spectral analysis of large-eddy simulations of the convective boundary layer. *J. Atmos. Sci.* **45**, 3573–3587 (1988).
55. Kang, M.-J., Chun, H.-Y. & Garcia, R. R. Role of equatorial waves and convective gravity waves in the 2015/2016 quasi-biennial oscillation disruption. *Atmos. Chem. Phys.* **20**, 14669–14693 (2020).
56. Lee, H.-K. et al. Characteristics of latent heating rate from GPM and convective gravity wave momentum flux calculated using the GPM data. *J. Geophys. Res. Atmos.* **127**, e2022JD037003 (2022).
57. Smith, I. H., Williams, P. D. & Schiemann, R. Clear-air turbulence trends over the North Atlantic in high-resolution climate models. *Clim. Dyn.* **60**, 1–7 (2023).
58. Kim, S.-H. et al. Retrieval of eddy dissipation rate from derived equivalent vertical gust included in Aircraft Meteorological Data Relay (AMDAR). *Atmos. Meas. Tech.* **13**, 1373–1385 (2020).

ACKNOWLEDGEMENTS

This research was supported by the Korea Meteorological Administration Research and Development Program under Grant KMI2022-00410 (H.-Y.C., J.-H.K., and S.-H.K.) and Basic Science Research Program through the National Research Foundation (NRF) of Korea funded by the Ministry of Education grant no. NRF-2022R111A1A01071708 (S.-H.K.) and grant no. NRF-2019R111A2A01060035 (J.-H.K.).

AUTHOR CONTRIBUTIONS

Conceptualization: S.-H.K., J.-H.K., H.-Y.C., and R.S. Methodology: S.-H.K. and J.-H.K. Investigation and visualization: S.-H.K. Supervision: J.-H.K. and H.-Y.C. Writing—original draft: S.-H.K. Writing—review and editing: J.-H.K., H.-Y.C., and R.S.

COMPETING INTERESTS

The authors declare no competing interests.

ADDITIONAL INFORMATION

Supplementary information The online version contains supplementary material available at <https://doi.org/10.1038/s41612-023-00421-3>.

Correspondence and requests for materials should be addressed to Soo-Hyun Kim or Jung-Hoon Kim.

Reprints and permission information is available at <http://www.nature.com/reprints>

Publisher's note Springer Nature remains neutral with regard to jurisdictional claims in published maps and institutional affiliations.



Open Access This article is licensed under a Creative Commons Attribution 4.0 International License, which permits use, sharing, adaptation, distribution and reproduction in any medium or format, as long as you give appropriate credit to the original author(s) and the source, provide a link to the Creative Commons license, and indicate if changes were made. The images or other third party material in this article are included in the article's Creative Commons license, unless indicated otherwise in a credit line to the material. If material is not included in the article's Creative Commons license and your intended use is not permitted by statutory regulation or exceeds the permitted use, you will need to obtain permission directly from the copyright holder. To view a copy of this license, visit <http://creativecommons.org/licenses/by/4.0/>.

© The Author(s) 2023